Ceramics International 49 (2023) 12758–12771

Contents lists available at ScienceDirect

Ceramics International

journal homepage: www.elsevier.com/locate/ceramint

One-step additive manufacturing of TiCp reinforced Al_2O_3–ZrO_2 eutectic ceramics composites by laser directed energy deposition

Dongjiang Wu [a], Xuexin Yu [a], Ziyuan Zhao [a], Guangyi Ma [a], Cong Zhou [b], Bi Zhang [b], Guanhui Ren [c,d], Fangyong Niu [a,*]

[a] Key Laboratory for Precision and Non-traditional Machining Technology of Ministry of Education, Dalian University of Technology, Dalian, 116024, Liaoning, PR China
[b] Department of Mechanical and Energy Engineering, Southern University of Science and Technology, Shenzhen, 518055, Guangdong, PR China
[c] Research and Development Department, Shenzhen Xinjinquan Precision Technology Co., Ltd., Shenzhen, 518055, Guangdong, PR China
[d] School of Mechanical Engineering, Shandong University, Jinan, 250061, Shandong, PR China

ARTICLE INFO

Keywords:
Additive manufacturing
Laser directed energy deposition
Al_2O_3–ZrO_2 eutectic ceramics
TiCp particles

ABSTRACT

With the rapid and adaptable process properties, laser directed energy deposition (LDED) is increasingly becoming popular for the direct additive manufacturing of melt growth eutectic composite ceramics. In this research, LDED is used to fabricate TiCp-reinforced Al_2O_3–ZrO_2 eutectic ceramics. The inhibitory mechanism of various ratios (0 wt % - 50 wt %) of TiCp on crack and porosity defects is investigated. In addition, a summary of the influence of TiCp on the microstructure and mechanical properties is provided. The results indicate that TiCp particles are uniformly distributed throughout the matrix, and the eutectic microstructure around TiCp exhibits an irregular eutectic transition as a result of a decrease in solidification rate. The mismatch of thermal expansion coefficient and elastic modulus between TiCp and Al_2O_3–ZrO_2 eutectic matrix causes the cracks to be pinned and transgranular, which suppresses the cracks effectively. Meanwhile, doping TiCp particles enhances the molten pool impact and increases the molten pool temperature, which accelerates the gas escape rate, leading to the porosity decreasing from 6.37% to 0.29%. In comparison to Al_2O_3–ZrO_2 eutectic ceramics, 50 wt% TiCp content results in the greatest flexural strength and fracture toughness, with increases of 34.18 and 13.42%, respectively. The greatest compressive strength is attained at 30 wt% TiCp doping, which is approximately 83.75% greater than eutectic ceramics.

1. Introduction

Al_2O_3–ZrO_2 eutectic ceramics are melt growth composites with a tightly bonded nano eutectic microstructure. Both at room temperature and at high temperatures, they exhibit good creep resistance and high temperature strength [1–10]. Therefore, Al_2O_3–ZrO_2 eutectic ceramics have the potential to be used as wear-resistant components, tailpipes, and heat shields [11–14]. Bridgman method [15], laser floating zone method [16], micro pulling down method [17,18], and edge defined film-fed [19] are among the typical techniques for preparing Al_2O_3–ZrO_2 eutectic ceramics. The limitations of these technologies include a high energy consumption, a complex procedure, and a lengthy preparation time.

LDED is an additive manufacturing technology that employs the laser as a high-energy heat source to effectively melt high melting point materials for deposition and shaping [20,21]. In recent years, LDED has become increasingly popular for the direct preparation of melt growth ceramics [22–26]. LDED enables the fabrication of samples in one-step without sintering, in contrast to traditional procedures. Therefore, shrinkage and deformation during sintering, as well as the entry of impurities such binder, are prevented. In addition, LDED is very adaptable in terms of component size, structure, and composition, and the fabricated samples are not constrained by the crucible, allowing for the quick manufacturing of composite materials and even functional gradient materials [27–29]. Due to the rapid melting and solidification of the material, the LDED fabrication process features a significant temperature gradient, which results in a complicated high-stress evolution inside the sample, causing defects such as cracks and porosity [30]. In response to these challenges, researchers have investigated process optimization [5,23,24,26,31] and combined ultrasonic-assisted [22,32] and

* Corresponding author.
E-mail address: niufangyong@dlut.edu.cn (F. Niu).

https://doi.org/10.1016/j.ceramint.2022.12.141
Received 21 October 2022; Received in revised form 5 December 2022; Accepted 14 December 2022
Available online 16 December 2022

high-temperature preheating [33–35] strategies to control both the characteristics and defects. Hu et al. [22] fabricated Al_2O_3–ZrO_2 bulk ceramics using ultrasound-assisted LDED and discovered that extra ultrasonic vibrations had the effect of grain refinement and crack suppression. Su et al. [26] manufactured Al_2O_3/$GdAlO_3$/ZrO_2 ternary eutectic ceramics via LDED with the assistance of both 700 °C substrate preheating and laser slow cooling to prevent cracks. However, the effect of these approaches diminishes as the sample height increases. Consequently, there is an urgent need to develop a method that operates constantly during the sample deposition process.

During the sintering preparation, researchers have added second phase particles, such as SiCp [36–39], TiCp [40], etc., to improve the characteristics of ceramics. Young et al. [41] created Al_2O_3–SiC tools using the hot-pressing sintering process and discovered that SiCp particles had a grain refinement effect, which considerably improved the cutting performance of tools. Bai et al. [42] doped Si_3N_4 particles into the Al_2O_3 matrix and found that cracks pinned or deflected at Si_3N_4 particles. In general, the rigid particles of the second phase have a larger elastic modulus than the matrix material. Besides, the distribution of rigid particles in the matrix causes crack pinning, transgranular and deflect, consequently preventing crack propagation and enhancing material. Therefore, the method of hard particle doping is promising to solve the defects in LDED fabricating melt growth ceramics.

The authors have employed SiCp particles to improve defects in Al_2O_3–ZrO_2 eutectic ceramics fabricated by LDED [43]. SiCp particles are shown to have a considerable influence on cracks and porosity inhibition, although the SiCp powder is poorly liquidity and the doping ratio is only 25 wt%. As the doping ratio keeps rising, the powder adsorbs to each other and forms clusters. Powder aggregation is comparable to porosity, which degrades the sample overall mechanical properties. Furthermore, the flexural strength of SiCp reinforced Al_2O_3–ZrO_2 eutectic sample decreases. Literature demonstrates [44,45] that TiCp particles have a low creep rate at high temperatures and grain boundary slip is not easily induced, hence contributing to the enhancement of the flexural strength of the ceramic matrix material. In terms of solidification process, SiCp sublimates directly at 1800 °C, therefore disintegrating into carbon and silicon-containing vapors during high temperature solidification, which severely restricts the material applicability in high temperature environments [43]. Studies have shown [46,47] that TiCp particles have an extraordinarily high melting point (3450 °C), and their hardness is second only to that of diamond. Additionally, great hardness and a low coefficient of friction are benefits of TiCp particles. In addition, the flowability of TiCp with the same particle size is superior to that of SiCp. This work thus proposes adding TiCp particles to Al_2O_3–ZrO_2 eutectic ceramic samples. LDED is used to fabricate Al_2O_3–ZrO_2 eutectic ceramics with varying TiCp contents, and the effect of TiCp particles on cracks, porosity, and mechanical properties is investigated.

2. Experimental conditions and method

2.1. Experimental equipment and materials

The experiment was conducted by LDED equipment shown in Fig. 1, which consisted of five parts: JK1002 Nd: YAG continuous laser, DPSF-2D powder feeder, CNC machine, industrial computer and circulating cooling water system. The laser with 1064 nm wavelength is delivered by optical fiber. During the experiment, high-purity argon (99.99% purity) supplied powder through a powder feeder to the tube and provided atmospheric protection for the deposition process.

Spherical Al_2O_3 powder (40–90 μm particle, Ya'an Bestry Performance Materials Corporation) and 8 wt% Y_2O_3 stabilized ZrO_2 powder (40–90 μm particle, Beijing Sunspraying New Materials Corporation) were used during LDED. No-spherical TiCp powder with the same particle size was purchased from Beijing Xingrongyuan Technology Corporation (Fig. 2). Fig. 3(a) depicts the XRD results of three powders, the principal constituents of which are listed in Tables 1–3. Before the experiment, the powder was dried for more than 4 h at 120 °C to assure its fluidity. Al_2O_3 and ZrO_2 powder were mechanically mixed in eutectic proportion (57.4 wt%: 42.6 wt%) prior to the addition of TiCp powder in proportions of 10 wt% (AZT10), 30 wt% (AZT30), 50 wt% (AZT50), 70 wt% (AZT70), and 90 wt% (AZT90). Fig. 3 (b) is the XRD pattern of

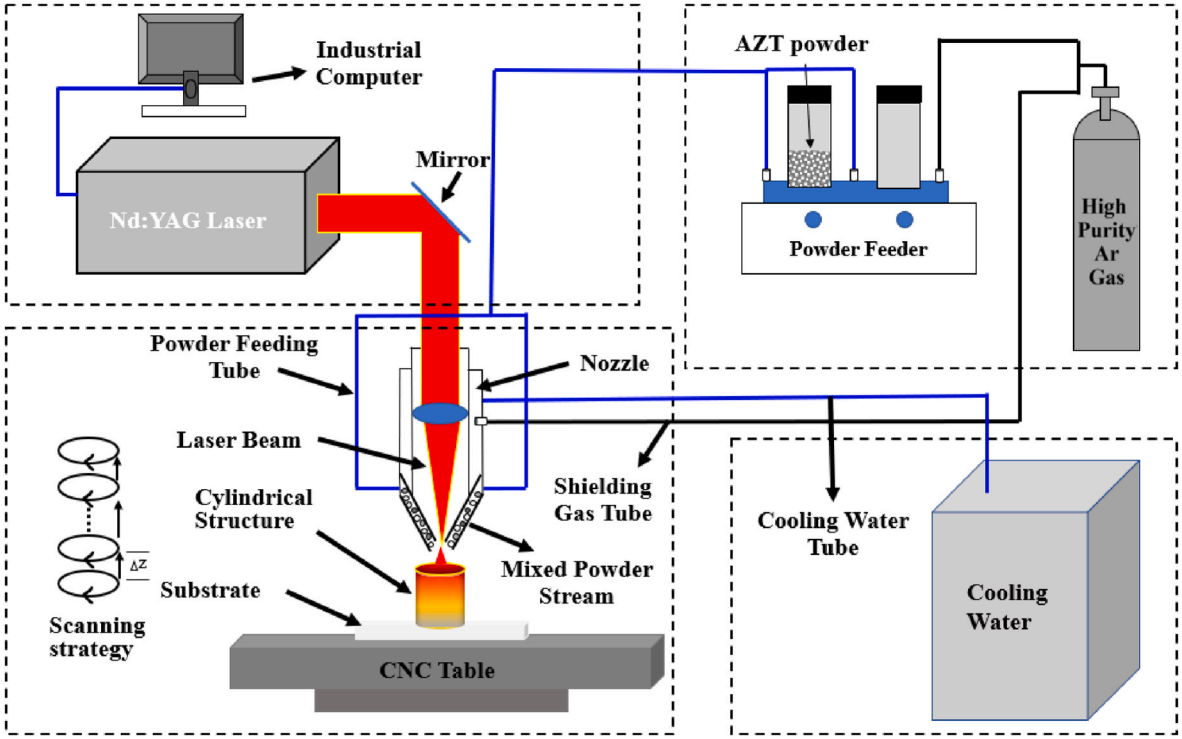

Fig. 1. LDED system.

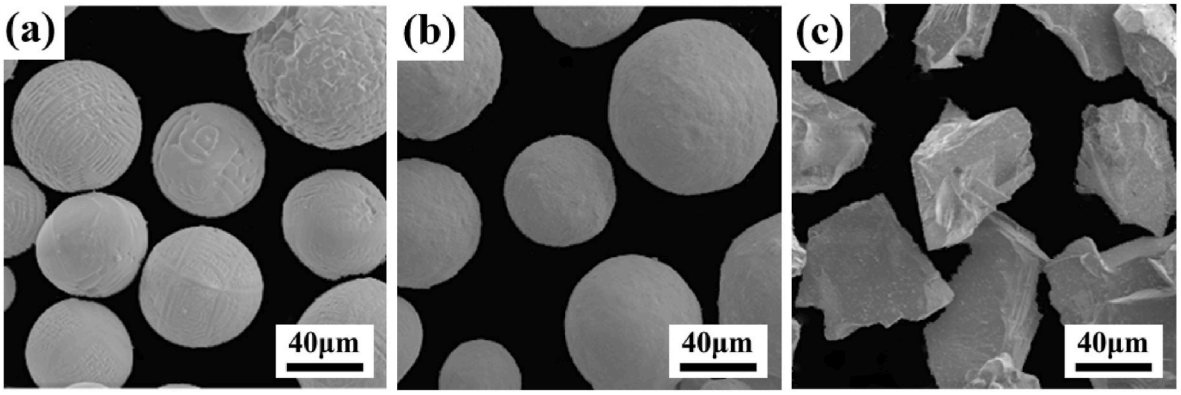

Fig. 2. Experimental materials: (a)Al_2O_3 powder; (b)ZrO_2 powder; (c)TiCp powder.

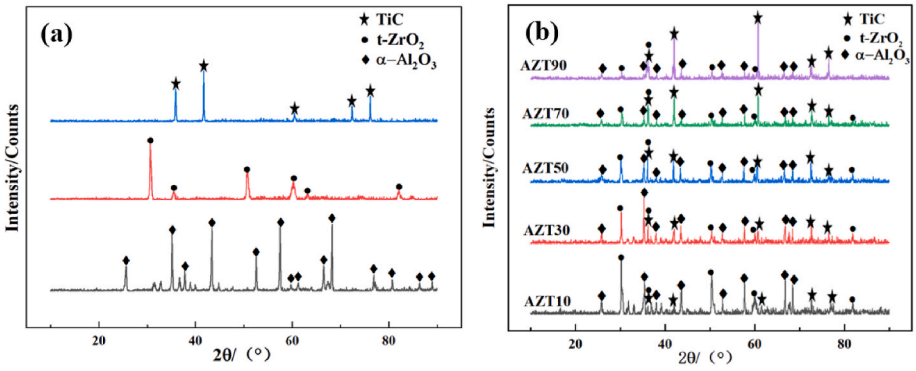

Fig. 3. XRD patterns of powders: (a) Al_2O_3, ZrO_2 and TiCp; (b) mixed powder.

Table 1
Composition and content of Al_2O_3 powder (wt.%).

Composition	Al_2O_3	SiO_2	Fe_2O_3	Na_2O	CaO
Content	>99.9	0.0041	0.0021	0.0014	<0.001

mixed powder. Considering the need to maintain good wettability and thermal expansion coefficient between sample and substrate, a hot-pressed sintered Al_2O_3 substrate (150 mm × 100 mm × 15 mm, 95% purity, Shanghai Xiyuan Industry Corporation) was used as the substrate in the experiments.

2.2. Experimental method

In this experiment, the following process parameters remained constant: laser power 340 W, scanning speed 400 mm/min, interlayer lift 0.4 mm, laser spot diameter 2 mm, and powder feeding rate 3.6 g/min. Cylindrical samples of Al_2O_3–ZrO_2 eutectic and AZT10, AZT30, AZT50, AZT70, AZT90 with 4 mm diameter and 36 mm deposition height were fabricated on the Al_2O_3 substrate. High-purity argon (99.99%) was used to deliver powder to substrate. The coaxially transmitted powder melted fast under the influence of the Nd:YAG laser beam, and the workstation lowered one layer lift Δz for every layer completed, depositing a total of ninety layers to finish the cylindrical sample. The height distance between the cladding head and the molten pool was kept as a constant during LDED.

2.3. Detection and analysis

After finishing the sample preparation, the longitudinal section of the sample was ground and polished by diamond grinding discs (400 #, 800 #, 1500 #, 2000 #, 3000 #) and 2.5 μm diamond grinding paste. Field emission scanning electron microscopy (SU5000) was utilized to analyze the microstructure of the materials, whilst the energy dispersive spectrometer (EDS) of the scanning electron microscopy was utilized to identify the type and proportion of elements in particular regions. X-ray diffraction (XRD-6000) was used to analyze the phase composition of powder and shaped samples. The target is a Cu target with operating voltage of 40 kV, operating current of 30 mA, diffraction angle of 2θ set to 10°~100° and scanning speed of 4°/min. The ratio of the pore area to the total cross-sectional area of the same deposition height cross-section was computed as porosity by using Image Pro Plus, and the average value for each set of three samples was determined. The longitudinal section of the polished sample was measured by Vickers hardness tester

Table 3
Composition and content of TiCp powder (wt.%).

Composition	TiC	Si/Ca	K/Na	Fe	Al
Content	>99.1	<0.01	<0.005	<0.09	<0.01

Table 2
Composition and content of ZrO_2 powder (wt.%).

Composition	ZrO_2	Y_2O_3	Al_2O_3	MgO	SiO_2	Fe_2O_3	CaO	Na_2O
Content	>90.3	7.5–8.5	<0.01	<0.01	<0.02	<0.002	<0.002	<0.01

with a load of 4.903 N and a dwell time of 15 s. The Vickers hardness was calculated by equation (1):

$$Hv = 1854.4 \times \frac{P}{d^2} \tag{1}$$

where Hv is the Vickers hardness (GPa), P is the loading force (N), and d is the arithmetic mean of two diagonals of the indentation (μm), where the average value of ten indentations was taken for each group of samples to obtain the microhardness. First, the elastic modulus of Al_2O_3–ZrO_2 eutectic composite ceramics with different TiCp content was evaluated by the rule of mixtures (ROM). For each proportion of samples, the upper and lower elastic moduli of the whole composite ceramics were obtained by Voigt (Equation (2)) [48] and Reuss (Equation (3)) [49] models. The calculated mean value of the upper and lower bounds of the elastic modulus was the overall elastic modulus. The modulus of elasticity of Al_2O_3–ZrO_2 eutectic ceramics at room temperature is 317.8 GPa, while that of TiCp is 470 GPa.

$$E^{up}_{Composite} = E_a V_a + E_m(1 - V_a) \tag{2}$$

$$\frac{1}{E^{low}_{Composite}} = \frac{V_a}{E_a} + \frac{1 - V_a}{E_m} \tag{3}$$

where $E^{up}_{Composite}$ is the upper bound of the elastic modulus of composite, $E^{low}_{Composite}$ is the lower bound of elastic modulus, E_a is the elastic modulus of TiCp, V_a is the volume fraction of TiCp (The calculation results are shown in Table 4), E_m is the elastic modulus of Al_2O_3–ZrO_2 eutectic ceramics, and the elastic modulus of the overall composite is calculated according to the upper and lower bound of the elastic modulus.

Since the cracks produced by the indentation are Palmqvist cracks, the fracture toughness of the composite ceramic material was calculated according to equation (4) [50]:

$$\left(\frac{K_{IC}\varphi}{HV\sqrt{d}}\right)\left(\frac{HV}{E_c\varphi}\right)^{0.4} = 0.035\left(\frac{l}{a}\right)^{-1/2} \tag{4}$$

where K_{IC} is the fracture toughness (MPa·m$^{1/2}$), Φ is the shape constraint factor ($\Phi \approx 3$), E_c is the elastic modulus of the composite (GPa), l is the Babbitt crack length (μm), and a is the half length of indentation diagonal (μm).

The three-point flexural test (GBT 6569-2006) was performed to measure the sample flexural strength. The cylindrical sample was ground into a rectangle sample with a cross-sectional dimension of 3 mm × 4 mm for the flexure test, where span was 30 mm and movement speed of the pressing head was 0.5 mm/min, and the flexural strength of the sample was calculated according to equation (5):

$$\sigma_f = \frac{3FL}{2bd^2} \tag{5}$$

where F is the maximum load (N), L is the span (mm), b is the fracture width (mm), and d is the fracture thickness (mm).

In the universal mechanical properties testing equipment (WDW-20E) used to measure the compression strength of the sample (GBT 8489-2006), the sample size was Φ5 × 12.5 mm and the pressing head moved at 0.2 mm/min. Calculation of compression strength based on equation (6).

Table 4
Volume fraction of composite TiCp.

Group	TiCp mass fraction	TiCp volume fraction
AZT10	10%	9.39%
AZT30	30%	28.56%
AZT50	50%	48.27%

$$\sigma_c = \frac{P}{A} \tag{6}$$

where P is the maximum load (N) and A is the cross-sectional area of the sample ($A = \pi d^2/4$, mm^2). The final figures for flexural and compression strength are the average of ten samples.

3. Results and discussion

3.1. Macroscopic morphology and microstructure characteristics

3.1.1. Macroscopic morphology

Fig. 4 represents the macroscopic morphology of cylindrical samples with varying amounts of TiCp. In the mode of layer-by-layer deposition, the exterior surface of the sample exhibits interlayer bonding features. The color of TiCp-doped samples altered from milky white to yellowish-gray, and the phenomena of sticky powder is observed. When TiCp doping ratio is less than 50 wt%, the sample radius drops from 6.63 mm to 5.42 mm as the TiCp content increases. When the content of TiCp exceeded 50 wt% (AZT70, AZT90), a great deal of smoke is produced during LDED, and the surface of sample is golden yellow (Fig. 4 (e), (f)). What's more, the surface roughness and shape accuracy have worsened dramatically. In addition, AZT70 and AZT90 have low strength and are extremely easy to fracture during removal from the substrate, with some powder flowing out (Fig. 5 (a)). As shown in Fig. 5 (b), the internal fracture of sample is a loose porous structure.

The XRD result (Fig. 5 (c)) indicates that the yellow matter on the surface of samples with a high proportion of TiCp (AZT70, AZT90) is composed of TiO_2. TiCp is extremely sensitive to the reaction depicted in equation (7) at high temperature aerobic circumstances, resulting in the oxidation of yellow TiO_2 sparse material, according to the findings of related research [51]. TiCp is a typical refractory transition metal carbide that occurs as unfused particles during LDED. When the TiCp ratio is too high, the TiCp in the sample's outer layer is exposed to air and oxidizes, causing the sample to become golden. In the fabrication process of Al_2O_3–ZrO_2 eutectic samples, the powder is melted by laser to form molten pool. However, when the surface tension of a molten pool cannot be balanced by gravity, the pool outflows to both sides, increasing the diameter of the sample. When the proportion of TiCp doping is lower than 50 wt%, the proportion of Al_2O_3–ZrO_2 eutectic powder utilized for melting to form the molten pool drops as the proportion of TiCp increases. The area of ceramics melt diffusion in the deposited layer decreases, resulting in the decrease of sample diameter. During the deposition process of the high percentage TiCp sample, TiCp particles impede the connection of the ceramics melt, and the interior of the sample is loose and porous. Therefore, a portion of the unfused TiCp particles are left in a dispersed state inside the sample, which contributes to its exceedingly low strength. As it is difficult for samples with a TiCp content above 50 wt% to fulfill the mechanical requirements of the majority of actual applications, only samples with a TiCp content below 50 wt% are discussed here.

$$2TiC(s) + 3O_2(g) = 2TiO_2(s) + 2CO(g) \tag{7}$$

3.1.2. Particle distribution and binding

Fig. 6 (a) shows the distribution features of TiCp particles in the sample, where TiCp particles are significantly concentrated inside the sample and less scattered at the boundaries. Fig. 6 (b)–(d) demonstrates that TiCp particles are spread equally throughout the matrix. As the TiCp ratio rises, the proportion of TiCp particles in the sample increases dramatically. In addition, the TiCp particles are well-defined and their boundary contains a white phase. This white phase comprises the components Al, Zr, O, as well as Ti and C, as seen in Fig. 7. Related studies have shown [43] that this white phase is the product of the interfacial reaction between particles and eutectic matrix, which possibly contributes to their interfacial bond strength.

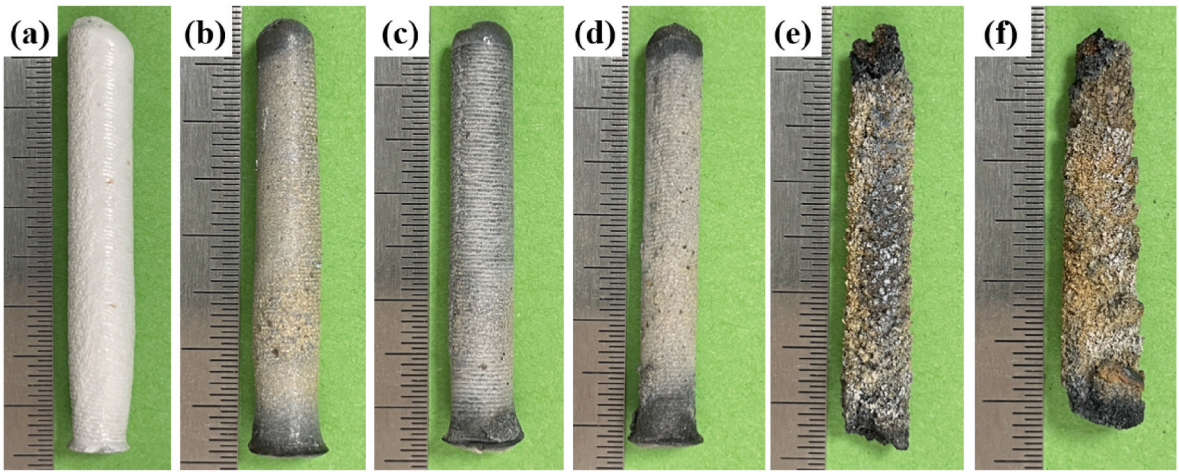

Fig. 4. Sample with different TiCp content: (a) Al_2O_3–ZrO_2 eutectic; (b) AZT10; (c) AZT30; (d) AZT50; (e) AZT70; (f) AZT90.

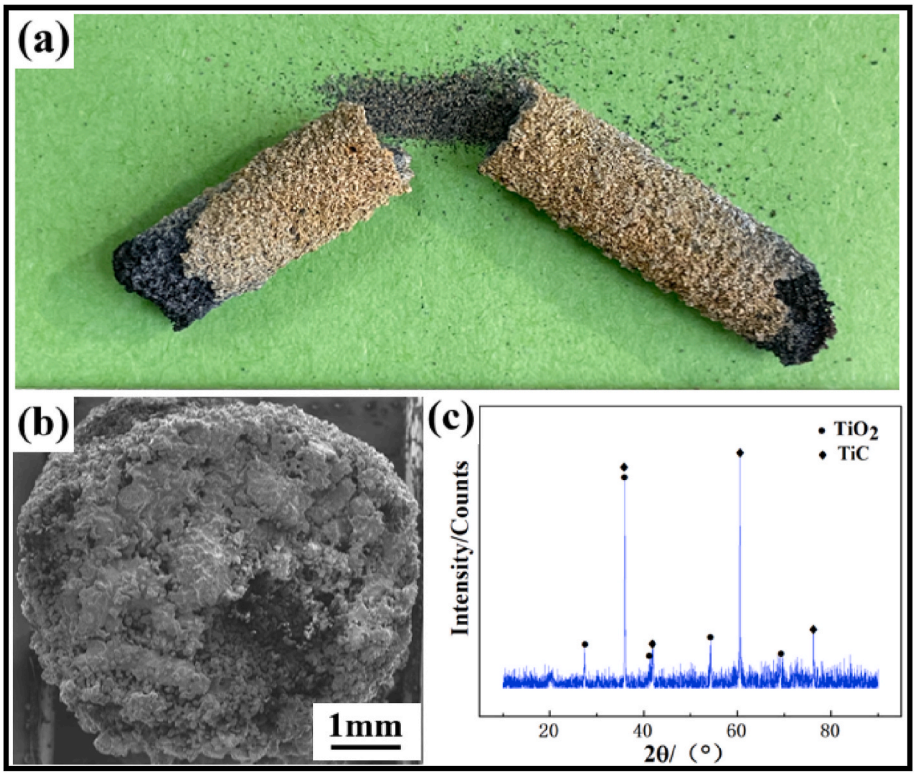

Fig. 5. Analysis of AZT70 sample:(a) AZT70 fracture sample; (b) Fracture diagram; (c) XRD pattern of yellow matter. (For interpretation of the references to color in this figure legend, the reader is referred to the Web version of this article.)

Related studies [52,53] have demonstrated that the particle distribution in the melt is mostly determined by the viscosity of the melt and the viscosity resistance of the liquid phase (Fig. 8). The Al_2O_3–ZrO_2 eutectic melt spreads around during LDED, so the melt pool is slightly larger in diameter than the scanning range of the laser. TiCp particles have a greater barrier to diffusion into the area beyond the laser scan, since the abrupt reduction in temperature increases the viscosity of the melt pool. In the region directly scanned by the laser, the temperature of the melt pool is higher, resulting in less resistance to the movement of the TiCp particles. In addition, due to the short solidification time, only a tiny number of TiCp particles are dispersed at the sample boundary prior to the solidification of the melt.

3.1.3. *Eutectic micrstructure*

Fig. 9 depicts the microstructure of Al_2O_3–ZrO_2 eutectic ceramics with varying TiCp doping ratios. As the proportion of TiCp increases, unmelted TiCp particles in the molten pool inhibit the formation of large crystal structures, resulting in a decrease in the size of the matrix crystal structure (Fig. 9 (a)–(c)). After doping with TiCp, dendritic eutectic begins to form around TiCp particles in AZT10 (Fig. 9 (b)). As the proportion of TiCp increases, the eutectic microstructure around TiCp particles eventually assumes an irregular form (Fig. 9 (d)).

The temperature of the two-phase eutectic point in the Al_2O_3–ZrO_2 binary eutectic phase diagram [54] is 1860 °C, and the eutectic composition is 57.4 wt% Al_2O_3 + 42.6 wt% ZrO_2. The growth mode of Al_2O_3–ZrO_2 eutectic structure under equilibrium conditions depends on the Jackson factor $\alpha = \Delta S_f/R$ (ΔS_f is the entropy of melting and R is the

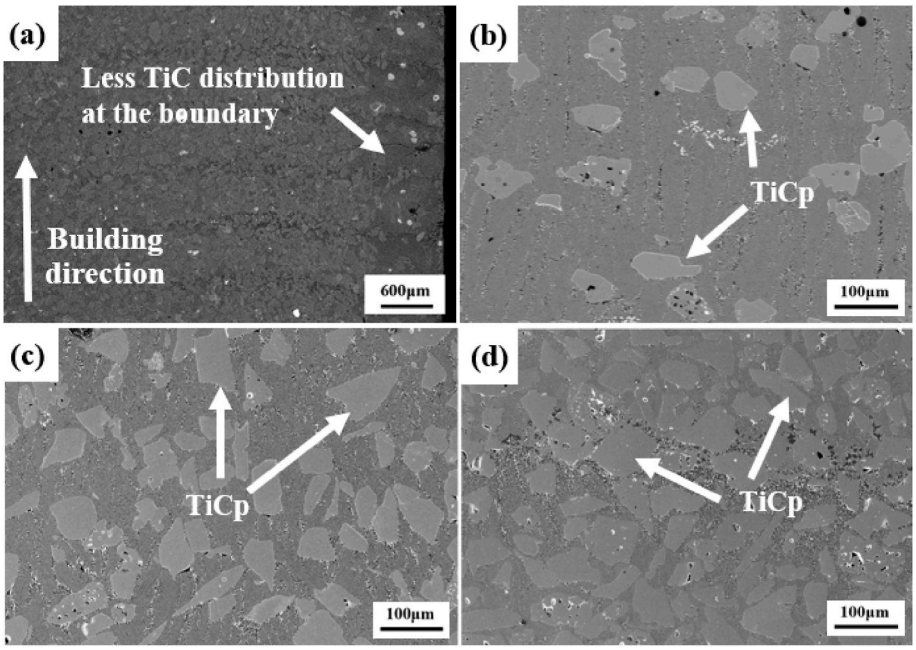

Fig. 6. Distribution of TiCp in the longitudinal section of the sample: (a) AZT30 sample longitudinal section; (b) AZT10; (c) AZT30; (d) AZT50.

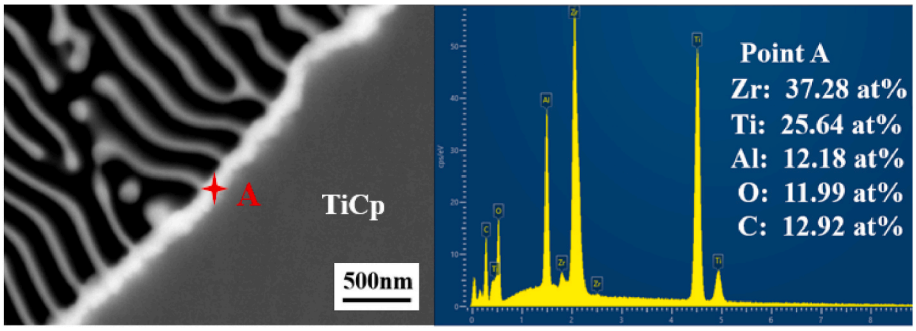

Fig. 7. TiCp particle boundary white phase EDS element detection.

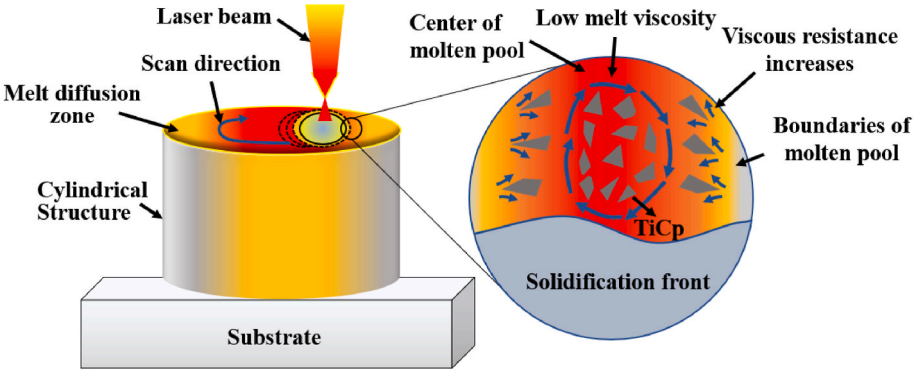

Fig. 8. Diagram of TiCp distribution.

gas constant.) [55], where the corresponding α values of Al_2O_3 and ZrO_2 are 5.7 and 3.5, respectively [56]. Due to Al_2O_3 phase grows in a faceted growth, while ZrO_2 phase grows in a non-faceted or weak faceted growth. At low solidification rates, Al_2O_3–ZrO_2 usually grows in a faceted/non-faceted way. These growth modes determine that Al_2O_3–ZrO_2 eutectic ceramics are facile in forming irregular or complex-regular eutectic microstructure [1]. However, the cooling rate of the LDED fabrication process is very fast, and the Al_2O_3 phase with a faceted microstructure turns into a rough interface, eventually leading to a lamellar or rod-shaped regular eutectic microstructure (Fig. 9 (a)) [57,58]. Extremely huge temperature differential exists at the bottom of the molten pool in the direction of deposition. During LDED, when heat is transferred to the substrate, crystals develop in the opposite direction of the heat flow to produce a columnar structure. According to

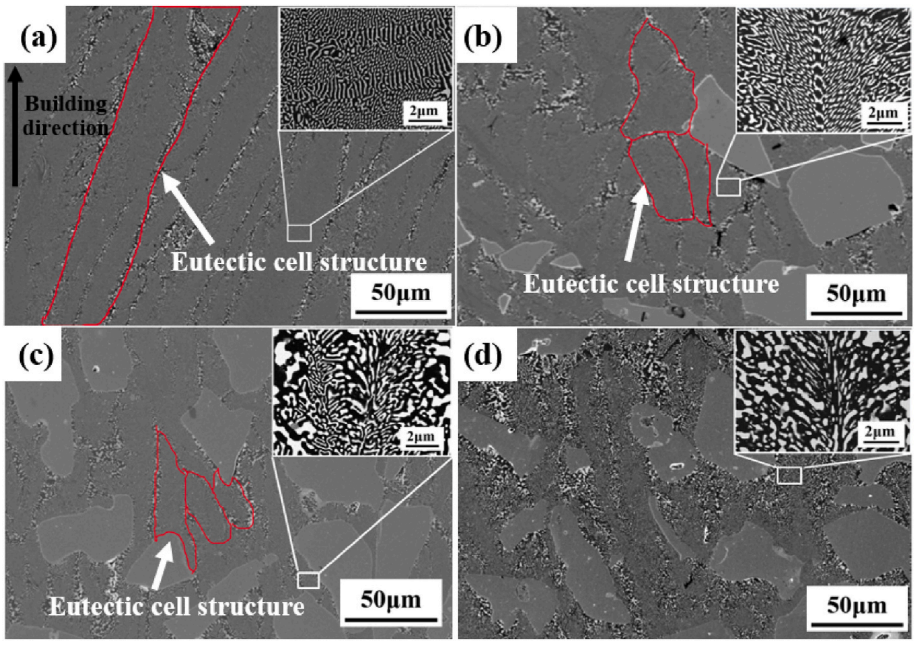

Fig. 9. Eutectic microstructure of samples with different TiCp doping ratios: (a) Al_2O_3–ZrO_2 eutectic; (b) AZT10; (c) AZT30; (d) AZT50.

Jackson-Hunt theory [59], the eutectic system grown under equilibrium conditions satisfies $\lambda^2 v = C$ (λ is the eutectic spacing, v is the growth rate, and C is the property constant) [18,55]. Al_2O_3–ZrO_2 eutectic ceramics exhibit submicron eutectic spacing as a result of the fast microstructure development rate v brought about by the rapid cooling of the samples during fabrication.

The temperature gradient at the solid-liquid interface is an important factor affecting the growth characteristics of the eutectic structure. TiCp particles form a low-energy solid-liquid interface in the molten pool, hence promoting the nucleation of eutectic microstructures and enhancing the nucleation rate. Near TiCp particles, Al_2O_3 and ZrO_2 phases are simpler to nucleate and develop in a dendritic eutectic manner. Dendritic eutectic transition of Al_2O_3–ZrO_2 eutectic structure occurs at this time. ZrO_2 phase embedded in Al_2O_3 phase (Fig. 9 (b)) [60] is symmetrically distributed in rod or fiber structure in dendritic eutectic. However, there is no obvious crystal transition zone in AZT50 (Fig. 9 (d)). As shown in Fig. 9 (d), when the TiCp content reaches 50 wt %, the majority of the eutectic microstructure is irregular. TiCp to Nd: YAG laser with an output wavelength of 1.06 nm has a higher absorption rate than oxides such as Al_2O_3 and ZrO_2 [61]. When the proportion of TiCp is too high, the rate of solidification of eutectic two phases between neighboring TiCp reduces dramatically. At low solidification rates, the eutectic two-phase diffusion distance is significantly greater than the layer spacing, and the eutectic coupling growth atoms diffuse adequately [1,62]. At this time, the solute concentration in the center of the eutectic phase differs from the solute concentration close to the three-phase point, therefore the development of the two eutectic phases is somewhat independent [63,64]. As seen in Fig. 9, The eutectic two phases grow independently nucleated from the melt and eventually form an irregular shape.

3.2. Mechanism of TiCp particles on porosity and cracks

3.2.1. Effect of TiCp doping on porosity

Porosity is one of the major defects in the LDED ceramic fabrication. The presence of pores in ceramics has a significant effect on their performance, which decreases the fracture toughness of ceramics on the one hand. In addition, the pores contribute to the formation of cracks during the fabrication process [65,66]. The relationship between porosity and TiCp doping ratio is shown in Fig. 10 (a). The addition of TiCp particles inhibits the pores inside Al_2O_3–ZrO_2 eutectic ceramics to a substantial degree. The average porosity of the Al_2O_3–ZrO_2 eutectic samples is 6.37%, and following doping with TiCp, the porosity of the samples decreases significantly. AZT10 has the lowest porosity among them at 0.29%. As the TiCp proportion continued to rise, the porosity increased marginally. Fig. 10 (b) depicts the pore distribution features in the

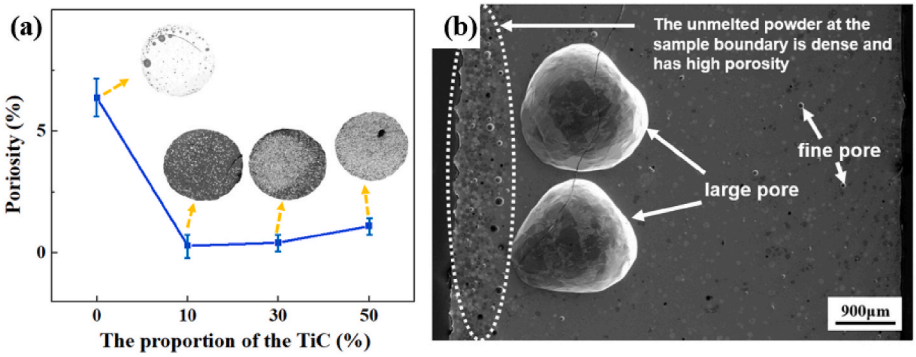

Fig. 10. Poriosity of AZT composite ceramics material: (a) Relationship between porosity and TiCp ratio; (b)Pores distribution characteristics of Al_2O_3–ZrO_2 eutectic samples.

longitudinal section of the Al_2O_3–ZrO_2 eutectic sample. Large pores are present within the sample, whereas pores of a smaller size are scattered near the boundary. Large pores no longer exist within AZT10 and AZT30, while tiny pores are still dispersed along the boundaries. AZT50 has large internal pores again.

During the deposition process, the pores form mostly because the gas cannot escape before the molten pool solidifies. There are three primary pore sources during LDED. Firstly, ceramics powders are transferred from high-purity argon to nozzles coaxial with the laser head, generating the molten pool under the action of the laser, and by the surface tension action of the molten pool, the powder transport a portion of the gas into the molten pool. Secondly, gas is contained inside the powder and escapes into the molten pool. Thirdly, certain impurities in the powder are gasified in the molten pool at a high temperature. These gases enter the molten pool and create bubbles that are unable to escape due to the fast cooling of the molten pool, causing porosity defects. There are a large number of dispersed powders outside the focus, which fall into the molten pool outside the laser radiation range, where the temperature of molten pool is lower. The ratio of molecules reaching the evaporated state on the surface of the melt decreases, and the gravitational force increases due to the shortening of the average molecular spacing, resulting in a higher surface tension. The powder impacts the tail of the molten pool, where the low temperature and high viscosity inhibit gas escape, leading in the formation of additional pores at the sample border.

The gas escape during LDED not only depends on the solidification rate of the molten pool, but also on the gas escape rate, which can be calculated from equation (8) [67]:

$$V_e = \frac{2g(\rho_L - \rho_G)r^2}{9\eta} \tag{8}$$

where V_e is the escape rate of the gas, g is the acceleration of gravity (m/s), ρ_L is the density of the molten pool (kg/m^3), ρ_G is the density of the gas (kg/m^3), r is the radius of bubble, and η is the viscosity of molten pool. From equation (8), the rate of gas spillage is inversely proportional to the viscosity of the molten pool, which is mainly calculated by equation (9) [67].

$$\eta = \eta_0 \exp\left(\frac{E + PV}{RT}\right) \tag{9}$$

where η_0 is a constant, E is the viscous flow activation energy, P is the pressure of molten pool, V is the volume of molten pool, R is the molar gas constant, and T is the temperature. This equation demonstrates that when the temperature of the molten pool increases, the viscosity decreases, which increases the rate of gas escape. Related studies [61] have shown that the absorption of Nd: YAG laser at an output wavelength of 1.06 μm by TiCp particles is greater than that of oxides such as Al_2O_3 and ZrO_2. So TiCp particles increase the absorption of the laser by the molten pool, which increases the temperature of the molten pool and thus accelerates the escape of gases. Meanwhile, TiCp persists as unfused particles with an irregular shape. During LDED process, TiCp particles puncture the bubbles in the molten pool, causing the gas within the bubbles to partially dissolve while the remaining gas escapes as tiny bubbles or remains in the sample to form pores. In addition, TiCp increases the impact of the molten pool and accelerates gas evacuation, hence lowering porosity [43,68] (Fig. 11).

The reaction of equation (10) [69] occurs between Al_2O_3 and TiCp at high temperature. This reaction is accompanied by the release of gases, which is inhibited by Y_2O_3 in ZrO_2 powder. The inhibition of equation (10) by Y_2O_3 is mainly due to the formation of solid solution by the added Y_2O_3, which is stable for TiCp and does not react chemically. Therefore, a stable phase composition exists between Al_2O_3 and TiCp, which prevents the chemical reaction between Al_2O_3 and TiCp [69]. However, when the proportion of TiCp doping exceeds 30 wt%, Y_2O_3 cannot be adequately distributed between Al_2O_3 and TiCp. Therefore, when the proportion of TiCp is considerable, Y_2O_3 cannot entirely prevent the interaction between Al_2O_3 and TiCp. The XRD results (Fig. 12) shows that diffraction peaks of the product TiO started to appear in AZT30, and the intensity of diffraction peaks of TiO increased significantly in AZT50. Lee et al. [70] discovered that samples also included TiO when TiCp doping was up to 30 wt%. During the fabrication of AZT50, as there is less liquid phase in the molten pool, the gas generated by the reaction is also less dissolved in the liquid phase. Therefore, AZT10 has the lowest porosity. Consequently, when the ratio of TiCp rises, the porosity of AZT50 increases somewhat, and bigger pores form inside the sample.

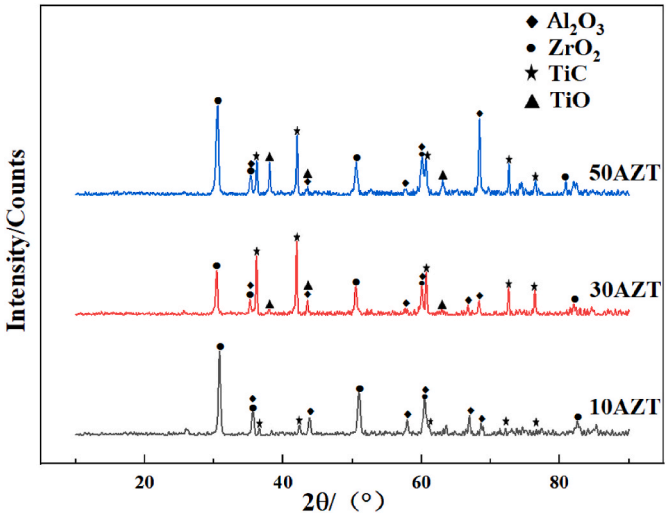

Fig. 12. XRD pattern of the sample.

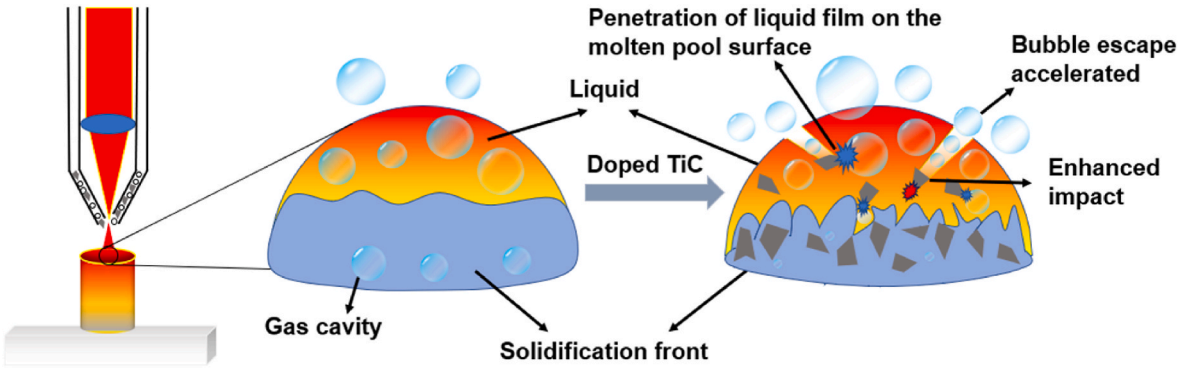

Fig. 11. Schematic diagram of pore suppression.

$$Al_2O_3 + TiC = Al_2O + TiO + CO \quad (10)$$

3.2.2. Effect of TiCp doping on crack

Cracking is difficult to suppress in LDED due to the high energy density of the laser beam and the inherent brittleness of ceramics, which severely restricts the application of ceramics remarkable high-temperature mechanical properties in different applications. Fig. 13 depicts the crack characteristics of samples obtained in this study with varying TiCp doping ratios. In the longitudinal section of Al_2O_3–ZrO_2 eutectic and AZT10, there are clearly visible longitudinal cracks. There are no longitudinal cracks in AZT30 as the TiCp concentration rises. However, minor transverse cracks existed in the region with less TiCp particle distribution near the boundary, whereas the longitudinal section of AZT50 included no visible cracks.

Cracking behavior of the sample is closely related to the stress distribution during LDED. The deposits fabricated by the sample are all based on the initial deposited layer, and cracks that not remelted and healed in the previous deposited layer have an important effect on the crack extension. During the cooling process, the current layer has a different temperature than the previous layer, resulting in tensile tension. Meanwhile, the unhealed crack tip in the first layer has a large stress concentration in the current layer, leading the crack to propagate and ultimately create a longitudinal crack beginning at the bottom of the sample [71]. There are also a few transverse cracks at the boundary of the sample. During cooling and solidification, the sample boundary is frequently subjected to increased tensile stress in the direction of deposition height, which leads to the propagation of transverse cracks to the center of the sample. However, when the crack expands to the area with dense TiCp particles in AZT30, the crack extends only at the boundary with a less dense TiCp particle distribution because TiCp impedes crack extension [72]. TiCp is densely distributed throughout the AZT50 sample, therefore TiCp particles placed near the crack source prevent the crack from spreading during the initial stage of crack formation, and thus no obvious cracks are observed inside AZT50.

The interaction between TiCp particles and cracks is seen in Fig. 14. When a crack propagates near TiCp particles, if it does not propagate sufficiently far to break the bond between TiCp and eutectic matrix, the crack becomes pinned to TiCp (Fig. 14 (a)). If the crack extension energy is greater, the crack extends further through the TiCp particles (Fig. 14 (b)). However, the consumed crack propagating energy shorten the distance of crack propagating.

TiCp is dispersed as unmelted particles in the matrix, while TiCp particles have higher fracture surface energy than matrix [73]. The mismatch of thermal expansion coefficient and elastic modulus between TiCp particles and Al_2O_3–ZrO_2 eutectic matrix are the primary causes of restraint cracking. Therefore, TiCp particles in Al_2O_3–ZrO_2 eutectic matrix are subjected to the force P as shown in equation (11) [74].

$$P = \frac{2\Delta\alpha\Delta T E_m}{(1+\nu_m) + 2\beta(1-2\nu_p)} \quad (11)$$

where $\Delta\alpha = \alpha_p - \alpha_m$ ($\Delta\alpha$ is the difference in thermal expansion coefficient; m, p subscripts denote matrix and particle), ν is the Poisson's ratio, E is modulus of elasticity, and $\triangle T$ is the temperature difference, $\beta = E_m/E_p$. This internal pressure creates a compressive stress σ_r in the matrix along the direction of the perpendicular particle surface and tensile stress σ_t tangential to the particle surface as follows [75].

$$\sigma_r = Pc^3 \quad (12)$$

$$\sigma_t = -\frac{1}{2}Pc^3 \quad (13)$$

where P is the internal pressure on the particle and c is the ratio of distance of the matrix from particle and the particle size. While the thermal expansion coefficient of TiCp is $7.74 \times 10^{-6}\,K^{-1}$, that of Al_2O_3 is $8.4 \times 10^{-6}\,K^{-1}$, and that of ZrO_2 is as high as $10.8 \times 10^{-6}\,K^{-1}$ [76]. From equation (11), $\Delta\alpha < 0$, so $P < 0$, $\sigma_r < 0$, and $\sigma_t > 0$. The Al_2O_3–ZrO_2 eutectic matrix is susceptible to compressive stress perpendicular to the surface direction of the particles and tensile stress tangential to the surface. Cracks at this stage are more likely to pinch the TiCp or penetrate the particles (Fig. 15). When the crack propagation energy is insufficient to destroy the bonding between TiCp and the Al_2O_3–ZrO_2 eutectic matrix, the crack is difficult to penetrate through the TiCp particles and be pinned to the surface or inside of TiCp particles (Fig. 14 (a)). When the crack propagation energy or external stress is high, transgranular occur (Fig. 14 (b)). However, transgranular fracture consume more crack propagation energy, which shortens the distance of crack propagation.

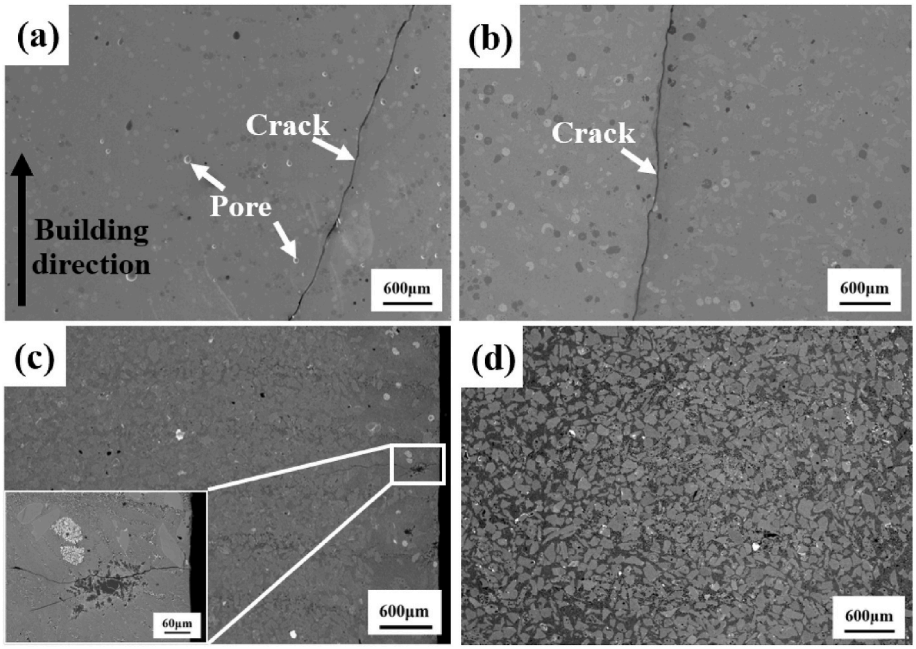

Fig. 13. Crack morphology in longitudinal section of different TiCp ratio samples: (a) Al_2O_3–ZrO_2 eutectic; (b) AZT10; (c) AZT30; (d) AZT50.

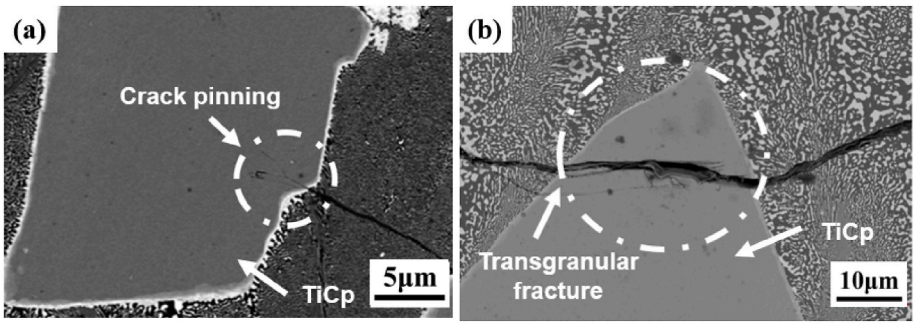

Fig. 14. TiCp crack suppression mechanism: (a) Crack pinning; (b) Transgranular fracture.

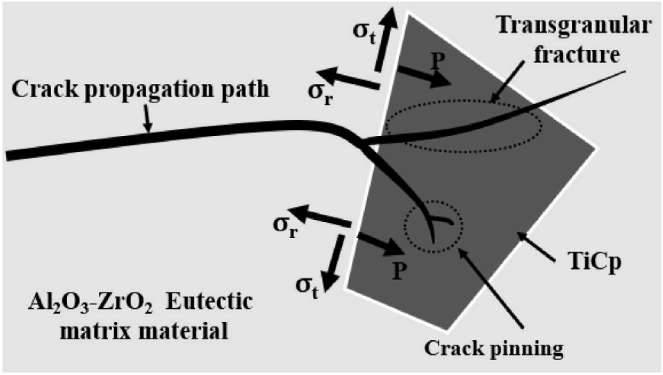

Fig. 15. Schematic diagram of crack extension.

3.3. Effect of TiCp particles on mechanical properties

3.3.1. Microhardness and fracture toughness

The variation of microhardness and fracture toughness of composite ceramics with TiCp ratio is shown in Fig. 16 (a). The microhardness of Al_2O_3–ZrO_2 eutectic matrix does not change significantly with the increase of TiCp content, ranging from 1693.43 HV to 1797.81 HV. However, the hardness of the TiCp particles distributed in the matrix is 2482.35 HV, which is significantly greater than that of eutectic matrix. The crack generated by Vickers indentation extends diagonally around the indentation. The crack and indentation measured by Image Pro Plus satisfy the relationship of $0.25 \leq (c\text{-}a)/a \leq 2.5$ (where a is the indent diagonal, c is the radial crack size), indicating that it is the indentation crack for Palmqvist. According to Equation (4), the fracture toughness of ceramics with various TiCp proportions is computed. The results indicate that the fracture toughness of composite ceramics rises steadily with increasing TiCp doping, with the fracture toughness of AZT50 reaching 4.14 ± 0.19 MPa $m^{1/2}$, a 13.42% increase. TiCp-reinforced particles have a greater fracture surface energy than matrix, and indentation cracks prefer to terminate at TiCp particles (Fig. 16 (b)). The uniform distribution of TiCp in AZT composite ceramics is more favourable to crack pinning and transgranular fracture than in Al_2O_3–ZrO_2 eutectic ceramics (Fig. 14). Thus, the energy of crack extension is effectively absorbed to achieve the toughening effect. Likewise, as TiCp doping rises, the elastic elasticity of composite ceramics increases proportionally, and crack propagation requires a greater driving force. Consequently, the fracture toughness of AZT composite ceramics is greater than that of Al_2O_3–ZrO_2 eutectic ceramics.

3.3.2. Flexural strength

Fig. 17 shows the relationship between the flexural strength of composite ceramics and the content of TiCp measured by three-point flexural method. The average flexural strength of Al_2O_3–ZrO_2 eutectic ceramic samples is 168.43 ± 42.57 MPa, while the maximum flexural strength is 226 ± 17.13 MPa when the TiCp concentration is 50 wt%, representing an increase of 34.18%. According to Griffith's intensity theory [77]:

$$\sigma_f = \sqrt{\frac{2E\gamma_f}{\pi a}} \tag{14}$$

where σ_f is the flexural strength; E is the modulus of elasticity; γ_f is the fracture surface energy, which can be used to describe the energy consumed per unit area of crack propagation in the sample; and a is the crack size. Therefore, internal crack size, elastic modulus and fracture surface energy of the sample are three factors affecting the flexural strength.

Firstly, due to the existence of internal penetration cracks in AZT10, the fracture of the flexural test samples clearly demonstrates that AZT10 is broken along the cracks (Fig. 17 (b)). Consequently, the flexural strength of AZT10 is lower than that of Al_2O_3–ZrO_2 eutectic ceramics, and then it progressively increases as TiCp doping increases. As a result that the elastic modulus of TiCp particles is greater than that of Al_2O_3–ZrO_2 eutectic matrix, the elastic modulus of composite samples increases as the TiCp ratio increases. According to equation (14), the

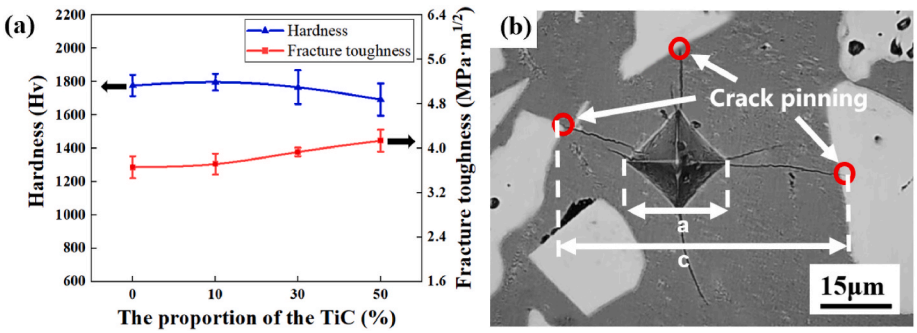

Fig. 16. Microhardness and fracture toughness of AZT composite ceramics material: (a) Microhardness and fracture toughness; (b) Vickers indentation micrograph.

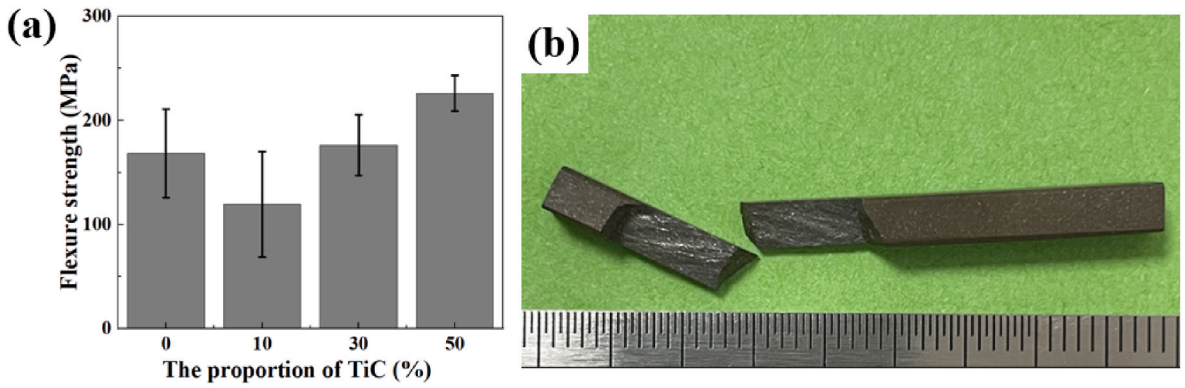

Fig. 17. Flexure strength of AZT composite ceramics material: (a) Flexural strength of different TiCp ratios; (b) Fracture shape of AZT10.

increase of elastic modulus contributes to improve the flexural strength of ceramics samples. On the fracture surface of AZT50, however, a high number of cleavage steps caused by transgranular fracture can be detected (Fig. 18 (a)). On the fracture surface, there is no visible plastic deformation, and there are still chips generated during the transgranular fracture of cleavage stage. EDS examination of the cleavage stages on the fracture surface (Fig. 18 (b)) reveals that the majority of the cleavage steps on the fracture surface are composed of TiCp. As a result, the more TiCp particles are doped, the more external work is required for the sample to fracture, and thus flexural increases with the increase of TiCp doping. Finally, the fracture surface energy γ_f of AZT samples with varying doping ratios is computed using equation (15) [78], which is discovered not to vary considerably. Thus, the increase in the overall flexural strength of ceramics is attributable to the increase in the elastic modulus, and the increase in the proportion of TiCp particles in the fracture cross-section causes more transgranular fracture, resulting in a greater energy consumption when the sample is fractured.

$$\gamma_f = \frac{K_{IC}^2}{2E} \tag{15}$$

3.3.3. Compressive strength

The variation of compression strength of the sample shown in Fig. 19 (a). The compressive strength of Al_2O_3–ZrO_2 eutectic ceramics is 261.64 ± 27.25 MPa, and Fig. 19 (b) demonstrates that the sample is broken along the crack. The highest compressive strength of AZT30 is 480.76 ± 63.74 MPa, which is 83.75% higher than that of Al_2O_3–ZrO_2 eutectic ceramics. When the amount of TiCp continues to increase, the compressive strength of AZT50 decreases significantly.

As shown in Fig. 20, during compression testing, the compressive load applied in the axial direction causes tensile stress in the radial direction of sample, which results in stress concentration at crack or pores inside the sample, leading to fracture or failure [79]. Usually, the crack propagates along the path with the minimum resistance it encounters.

During the compression test of Al_2O_3–ZrO_2 eutectic and AZT10, the tensile stress is concentrated at the crack in the sample. The microstructure with directional growth parallel to the building direction is more conducive to crack extension during the compression test, resulting in sample fracture along the crack at a relatively low load. The overall compressive strength of AZT50 can be explained by the empirical formula for strength/porosity [78].

$$\sigma_c = \sigma_0 \exp(-nQ) \tag{16}$$

where σ_c is compressive strength, σ_0 is strength of the composite when the porosity is 0, Q is porosity of the sample, and n is a constant. Firstly, large size pores appear in 50AZT, which leads to stress concentration at the pores during compression. In addition, the compression strength is intimately connected to the eutectic microstructure as well as the defects. When the TiCp content reaches 50 wt%, the amount of eutectic powder required for solidification declines, and the AZT50 structure consists primarily of coarse and irregular eutectic. It is evident that the eutectic spacing of this irregular eutectic structure is greater than that of AZT30, which results in a comparatively weak bonding of grain boundaries in AZT50 and makes it easier for the sample to slide and deform under compressive stress, ultimately leading to fracture [80–84].

4. Conclusion

In this paper, Al_2O_3–ZrO_2 eutectic ceramics samples with different TiCp content (0 wt% - 50 wt%) are prepared by LDED. The effects of doping TiCp on defects, microstructure, and mechanical properties are systematically studied. The research results present a novel strategy for the LDED fabrication of high-performance Al_2O_3–ZrO_2 eutectic ceramics. The primary results of the research are as follows:

(1) The introduction of TiCp particles reduces the size of the columnar crystal cluster in Al_2O_3–ZrO_2 eutectic ceramics. In the

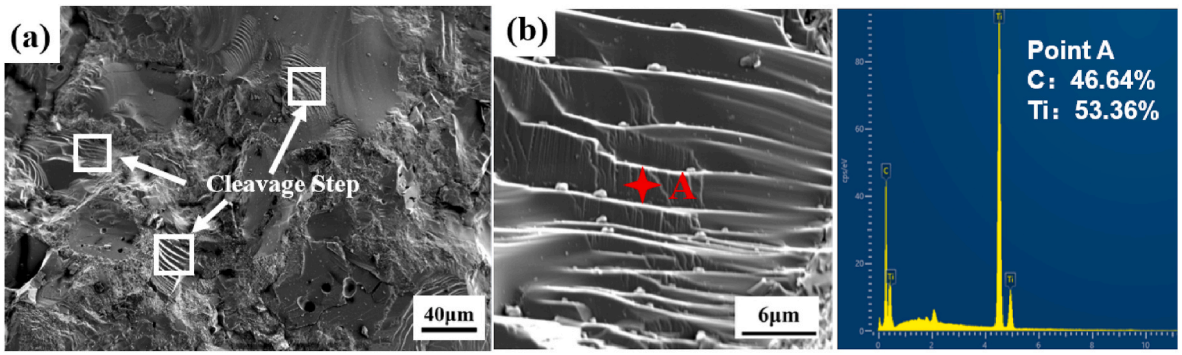

Fig. 18. Fracture of AZT50 sample: (a) micromorphology of fracture; (b) EDS element analysis of cleavage step.

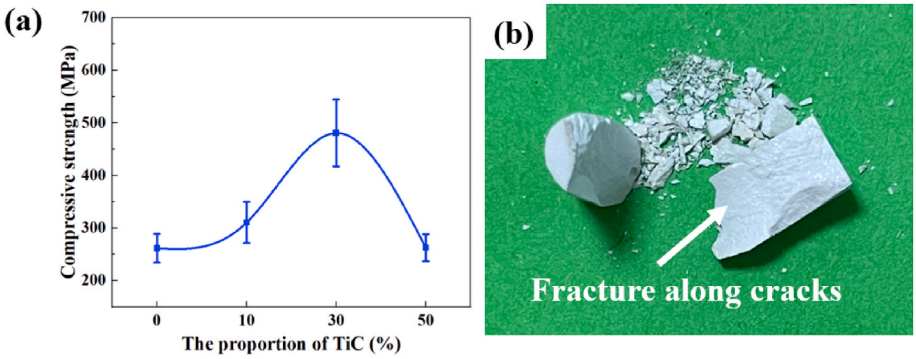

Fig. 19. Compressive strength of AZT composite ceramics material: (a) Compression strength of samples with different TiCp ratios; (b) Fracture of sample after compression.

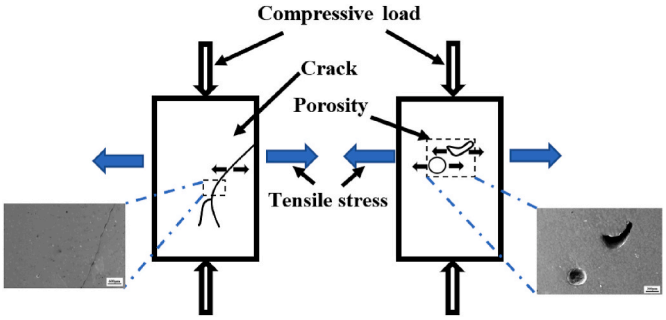

Fig. 20. Schematic diagram of compression experiment.

process of nucleation and crystallization, it destabilizes the two eutectic phases, and the eutectic microstructure begins to transition into irregular. The change in eutectic microstructure is due to the decrease in eutectic melt solidification rate caused by the increase in TiCp content;

(2) The doping of TiCp particles significantly inhibits the porosity and cracks of Al_2O_3–ZrO_2 eutectic ceramics. The porosity drops dramatically after TiCp doping, falling from 6.37% to 0.29%. The primary cause is that the addition of TiCp particles raises the temperature of the molten pool and intensifies the disturbance, hence accelerating the gas escape rate and decreasing the porosity. Moreover, doping TiCp particles causes the mismatch of thermal expansion coefficient and elastic modulus with Al_2O_3–ZrO_2 eutectic matrix. The residual stress field around TiCp particles interacts with the tip of the propagating crack, making the crack transgranular and pinning, so as to achieve the effect of crack suppression;

(3) The microhardness of Al_2O_3–ZrO_2 eutectic matrix changes little with the increase of TiCp doping ratio, but the fracture toughness gradually increases with the increase of TiCp ratio. TiCp particles have a greater elastic modulus and a lower thermal expansion coefficient than matrix material. AZT50 has the maximum flexural strength, up to 226 MPa. The increase in elastic modulus and transgranular fracture generated by TiCp particles is the primary reason for the requirement to increase the external work. The compressive load applied axially during the compression test causes tensile stress in the radial direction of the sample, resulting in stress concentration around cracks or porosity defects, which eventually lead to sample fragmentation. AZT30 has the highest compressive strength of 480.76 MPa since it has fewest internal defects.

Declaration of competing interest

The authors declare that they have no known competing financial interests or personal relationships that could have appeared to influence the work reported in this paper.

Acknowledgments

This work was funded by the National Natural Science Foundation of China (Nos. 51805070, 51790172, 52175291), the Fundamental Research Funds for the Central Universities (No. DUT22YG210, DUT22LAB117). And the authors also gratefully acknowledge the financial support from the Shenzhen Science and Technology Innovation Commission for the project numbered as JSGG20210420091802007.

References

[1] J. Llorca, V.M. Orera, Directionally solidified eutectic ceramic oxides, Prog. Mater. Sci. 51 (2006) 711–809, https://doi.org/10.1016/j.pmatsci.2005.10.002.

[2] M.C. Mesa, P.B. Oliete, J.Y. Pastor, A. Martin, J. Llorca, Mechanical properties up to 1900 K of Al_2O_3/$Er_3Al_5O_{12}$/ZrO_2 eutectic ceramics grown by the laser floating zone method, J. Eur. Ceram. Soc. 34 (2014) 2081–2087, https://doi.org/10.1016/j.jeurceramsoc.2013.11.013.

[3] H.J. Su, J. Zhang, K. Song, L. Liu, H.Z. Fu, Investigation of the solidification behavior of Al_2O_3/YAG/YSZ ceramic in situ composite with off-eutectic composition, J. Eur. Ceram. Soc. 31 (2011) 1233–1239, https://doi.org/10.1016/j.jeurceramsoc.2010.06.011.

[4] J.Y. Pastor, P. Poza, J. Llorca, J.I. Peña, R.I. Merino, V.M. Orera, Mechanical properties of directionally solidified Al_2O_3–ZrO_2(Y_2O_3) eutectics, Mater. Sci. Eng. A-Struct. Mater. Prop. Microstruct. Process. 308 (2001) 241–249, https://doi.org/10.1016/S0921-5093(00)02040-2.

[5] J.M. Pappas, A.R. Thakur, X.Y. Dong, Effects of zirconia doping on additively manufactured alumina ceramics by laser direct deposition, Mater. Des. 192 (2020), 108711, https://doi.org/10.1016/j.matdes.2020.108711.

[6] X. Wang, W. Zhang, Y.J. Zhong, L.C. Sun, Q.D. Hu, J.Y. Wang, Introduction of low strain energy $GdAlO_3$ grain boundaries into directionally solidified Al_2O_3/$GdAlO_3$ eutectics, Acta Mater. 221 (2021), 117355, https://doi.org/10.1016/j.actamat.2021.117355.

[7] X. Wang, W.S. Xiang, Y.J. Zhong, L. Wan, F.X. Yan, Q.G. Xian, B.L. Jiang, J. Y. Wang, Preferential growth of directionally solidified Al_2O_3/$SmAlO_3$ eutectic ceramics, Scripta Mater. 187 (2020) 424–427, https://doi.org/10.1016/j.scriptamat.2020.06.069.

[8] Z.Q. Fan, Y.T. Zhao, Q.Y. Tan, N. Mo, M.X. Zhang, M.Y. Lu, H. Huang, Nanostructured Al_2O_3-YAG-ZrO_2 ternary eutectic components prepared by laser engineered net shaping, Acta Mater. 170 (2019) 24–37, https://doi.org/10.1016/j.actamat.2019.03.020.

[9] Z.Q. Fan, Y.T. Zhao, Q.Y. Tan, B.W. Yu, M.X. Zhang, H. Huang, New insights into the growth mechanism of 3D-printed Al_2O_3–$Y_3Al_5O_{12}$ binary eutectic composites, Scripta Mater. 178 (2020) 274–280, https://doi.org/10.1016/j.scriptamat.2019.11.040.

[10] X. Wang, N. Zhang, Y.J. Zhong, B.L. Jiang, L.H. Lou, J. Zhang, J.Y. Wang, Microstructure evolution and crystallography of directionally solidified Al_2O_3/$Y_3Al_5O_{12}$ eutectic ceramics prepared by the modified Bridgman method, J. Mater. Sci. Technol. 35 (2019) 1982–1988, https://doi.org/10.1016/j.jmst.2019.05.018.

[11] L. Guo, H. Xin, Z. Zhang, X.M. Zhang, F.X. Ye, Microstructure modification of Y_2O_3 stabilized ZrO_2 thermal barrier coatings by laser glazing and the effects on the hot corrosion resistance, J. Adv. Ceram. 9 (2020) 232–242, https://doi.org/10.1007/s40145-020-0363-z.

[12] Y.N. Guo, H.J. Su, H.T. Zhou, Z.L. Shen, Y. Liu, J. Zhang, Unique strength-ductility balance of AlCoCrFeNi2.1 eutectic high entropy alloy with ultra-fine duplex microstructure prepared by selective laser melting, J. Mater. Sci. Technol. 111 (2022) 298–306, https://doi.org/10.1016/j.jmst.2021.10.013.
[13] Z.L. Shen, H.J. Su, H.F. Liu, D. Zhao, Y. Liu, Y.N. Guo, Directly fabricated Al_2O_3/$GdAlO_3$ eutectic ceramic with large smooth surface by selective laser melting: rapid solidification behavior and thermal field simulation, J. Eur. Ceram. Soc. 42 (2022) 1088–1101, https://doi.org/10.1016/j.jeurceramsoc.2021.11.003.
[14] H.F. Liu, H.J. Su, Z.L. Shen, D. Zhao, Y. Liu, Y.N. Guo, Insights into high thermal stability of laser additively manufactured Al_2O_3/$GdAlO_3$/ZrO_2 eutectic ceramics under high temperatures, Addit. Manuf. 48 (2021), 102425, https://doi.org/10.1016/j.addma.2021.102425.
[15] Y. Waku, N. Nakagawa, H. Ohtsubo, A. Mitani, K. Shimizu, Fracture and deformation behaviour of melt growth composites at very high temperatures, J. Mater. Sci. 36 (2001) 1585–1594, https://doi.org/10.1023/A:1017519113164.
[16] H.J. Su, J. Zhang, L. Liu, H.Z. Fu, Growth characteristics of directionally solidified Al_2O_3/YAG/ZrO_2 ternary hypereutectic in situ composites under ultra-high temperature gradient, Int. J. Miner. Metall. Mater. 18 (2011) 121–125, https://doi.org/10.1007/s12613-011-0410-4.
[17] J.H. Lee, A. Yoshikawa, H. Kaiden, K. Lebbou, T. Fukuda, D.H. Yoon, Y. Waku, Microstructure of Y_2O_3 doped Al_2O_3/ZrO_2 eutectic fibers grown by the micro-pulling-down method, J. Cryst. Growth 231 (2001) 179–185, https://doi.org/10.1016/S0022-0248(01)01451-8.
[18] J.H. Lee, A. Yoshikawa, Y. Murayama, Y. Waku, S. Hanada, T. Fukuda, Microstructure and mechanical properties of Al_2O_3/$Y_3Al_5O_{12}$/ZrO_2 ternary eutectic materials, J. Eur. Ceram. Soc. 25 (2005) 1411–1417, https://doi.org/10.1016/j.jeurceramsoc.2005.01.034.
[19] D.Y. Park, J.M. Yang, Effect of the microstructure on the mechanical properties of a directionally solidified $Y_3Al_5O_{12}$/Al_2O_3 eutectic fiber, J. Mater. Sci. 36 (2001) 5593–5601, https://doi.org/10.1023/A:1012561531552.
[20] D.J. Wu, C.S. Yu, Q.Y. Wang, F.Y. Niu, G.Y. Ma, H. Wang, C. Zhou, B. Zhang, Synchronous-hammer-forging-assisted laser directed energy deposition additive manufacturing of high-performance 316L samples, J. Mater. Process. Technol. 307 (2022), 117695, https://doi.org/10.1016/j.jmatprotec.2022.117695.
[21] D.D. Gu, X.Y. Shi, R. Poprawe, D.L. Bourell, R. Setchi, J.H. Zhu, Material-structure-performance integrated laser-metal additive manufacturing, Science 372 (2021) 6545, https://doi.org/10.1126/science.abg148.
[22] Y.B. Hu, F.D. Ning, W.L. Cong, Y.C. Li, X.L. Wang, H. Wang, Ultrasonic vibration-assisted laser engineering net shaping of ZrO_2-Al_2O_3 bulk parts: effects on crack suppression, microstructure, and mechanical properties, Ceram. Int. 44 (2018) 2752–2760, https://doi.org/10.1016/j.ceramint.2017.11.013.
[23] J.M. Pappas, A.R. Thakur, E.C. Kinzel, X.Y. Dong, Direct 3D printing of transparent magnesium aluminate spinel ceramics, J. Laser Appl. 33 (2021), 12018, https://doi.org/10.2351/7.0000327.
[24] J.M. Pappas, E.C. Kinzel, X.Y. Dong, Laser direct deposited transparent magnesium aluminate spinel, Manuf. Lett. 24 (2020) 92–95, https://doi.org/10.1016/j.mfglet.2020.04.003.
[25] Z.Q. Fan, Y.T. Zhao, M.Y. Lu, H. Huang, Yttria stabilized zirconia (YSZ) thin wall structures fabricated using laser engineered net shaping (LENS), Int. J. Adv. Manuf. Technol. 105 (2019) 4491–4498, https://doi.org/10.1007/s00170-019-03322-z.
[26] H.F. Liu, H.J. Su, Z.L. Shen, D. Zhao, Y. Liu, Y.N. Guo, Preparation of large-size Al_2O_3/$GdAlO_3$/ZrO_2 ternary eutectic ceramic rod by laser directed energy deposition and its microstructure homogenization mechanism, J. Mater. Sci. Technol. 85 (2021) 218–223, https://doi.org/10.1016/j.jmst.2021.01.025.
[27] D.J. Wu, J. Shi, F.Y. Niu, G.Y. Ma, C. Zhou, B. Zhang, Direct additive manufacturing of melt growth Al_2O_3-ZrO_2 functionally graded ceramics by laser directed energy deposition, J. Eur. Ceram. Soc. 42 (2022) 2957–2973, https://doi.org/10.1016/j.jeurceramsoc.2022.01.034.
[28] K. Shah, I.U. Haq, A. Khan, S.A. Shah, M. Khan, A.J. Pinkerton, Parametric study of development of Inconel-steel functionally graded materials by laser direct metal deposition, Mater. Des. 54 (2014) 531–538, https://doi.org/10.1016/j.matdes.2013.08.079.
[29] C. Schneider-Maunoury, L. Weiss, P. Acquier, D. Boisselier, P. Laheurte, Functionally graded Ti_6Al_4V-Mo alloy manufactured with DED-CLAD® process, Addit. Manuf. 17 (2017) 55–56, https://doi.org/10.1016/j.addma.2017.07.008.
[30] Z. Chen, X.H. Sun, Y.P. Shang, K.Z. Xiong, Z.K. Xu, R.S. Guo, Dense ceramics with complex shape fabricated by 3D printing: a review, J. Adv. Ceram. 10 (2021) 195–218, https://doi.org/10.1007/s40145-020-0444-z.
[31] F.Z. Li, X.W. Zhang, C.Y. Sui, J.Z. Wu, H.Y. Wei, Y. Zhang, Microstructure and mechanical properties of Al_2O_3-ZrO_2 ceramic deposited by laser direct material deposition, Ceram. Int. 44 (2018) 18960–18968, https://doi.org/10.1016/j.ceramint.2018.07.135.
[32] S. Yan, D.J. Wu, F.Y. Niu, Y.F. Huang, N. Liu, G.Y. Ma, Effect of ultrasonic power on forming quality of nano-sized Al_2O_3-ZrO_2 eutectic ceramic via laser engineered net shaping (LENS), Ceram. Int. 44 (2018) 1120–1126, https://doi.org/10.1016/j.ceramint.2017.10.067.
[33] Q. Liu, Y. Danlos, B. Song, B.C. Zhang, S. Yin, H.L. Liao, Effect of high-temperature preheating on the selective laser melting of yttria-stabilized zirconia ceramic, J. Mater. Process. Technol. 222 (2015) 61–74, https://doi.org/10.1016/j.jmatprotec.2015.02.036.
[34] Z. Liu, K. Song, B. Gao, H.O. Yang, W.D. Huang, Microstructure and mechanical properties of Al_2O_3/ZrO_2 directionally solidified eutectic ceramic prepared by laser 3D printing, J. Mater. Sci. Technol. 32 (2016) 320–325, https://doi.org/10.1016/j.jmst.2015.11.017.
[35] H.J. Su, J. Zhang, L. Liu, J. Eckert, H.Z. Fu, Rapid growth and formation mechanism of ultrafine structural oxide eutectic ceramics by laser direct forming, Appl. Phys. Lett. 99 (2011), 221913, https://doi.org/10.1063/1.3664108.
[36] A. Henniche, J.H. Ouyang, Z.G. Liu, Y.H. Ma, Z.G. Wang, Y.J. Wang, Effect of SiC addition on mechanical properties of hot-pressed Al_2O_3-$GdAlO_3$ ceramics with eutectic composition, Ceram. Int. 44 (2018) 9585–9592, https://doi.org/10.1016/j.ceramint.2018.02.182.
[37] Y.L. Dong, F.M. Xu, X.L. Shi, C. Zhang, Z.J. Zhang, J.M. Zhang, Fabrication and mechanical properties of nano-/micro-sized Al_2O_3/SiC composites, Mater. Sci. Eng. A-Struct. Mater. Prop. Microstruct. Process 504 (2009) 49–54, https://doi.org/10.1016/j.msea.2008.10.021.
[38] A. Demir, Z. Tatli, Mechanical property improvements in Nicalon SiC fibre reinforced silicon nitride ceramics by oxide coating of Si_3N_4 starting powders, Compos. Appl. Sci. Manuf. 35 (2004) 1433–1440, https://doi.org/10.1016/j.compositesa.2004.05.007.
[39] A. Jalowiecki, J. Bill, F. Aldinger, J. Mayer, Interface characterization of nanosized B-doped Si_3N_4/SiC ceramics, Compos. Appl. Sci. Manuf. 27 (1996) 717–721, https://doi.org/10.1016/1359-835X(96)00004-8.
[40] M.L. Cheng, H.L. Liu, B. Zhao, C.Z. Huang, P. Yao, B. Wang, Mechanical properties of two types of Al_2O_3/TiC ceramic cutting tool material at room and elevated temperatures, Ceram. Int. 43 (2017) 13869–13874, https://doi.org/10.1016/j.ceramint.2017.07.110.
[41] Y.M. Ko, W.T. Kwon, Y.W. Kim, Development of Al_2O_3–SiC composite tool for machining application, Ceram. Int. 30 (2004) 2081–2086, https://doi.org/10.1016/j.ceramint.2003.11.011.
[42] X.L. Bai, C.Z. Huang, J. Wang, B. Zou, H.L. Liu, Fabrication and characterization of Si_3N_4 reinforced Al_2O_3-based ceramic tool materials, Ceram. Int. 41 (2015) 12798–12804, https://doi.org/10.1016/j.ceramint.2015.06.115.
[43] D.J. Wu, F. Lu, D.K. Zhao, G.Y. Ma, C.J. Li, J. Ding, Effect of doping SiC particles on cracks and pores of Al_2O_3–ZrO_2 eutectic ceramics fabricated by directed laser deposition, J. Mater. Sci. 54 (2019) 9321–9330, https://doi.org/10.1007/s10853-019-03555-z.
[44] N. Liu, M. Shi, Y.D. Xu, X.Q. You, P.P. Ren, J.P. Feng, Effect of starting powders size on the Al_2O_3–TiC composites, Int. J. Refract. Metals Hard Mater. 22 (2004) 265–269, https://doi.org/10.1016/j.ijrmhm.2004.09.001.
[45] M.L. Cheng, H.L. Liu, B. Zhao, C.Z. Huang, P. Yao, B. Wang, Mechanical properties of two types of Al_2O_3/TiC ceramic cutting tool material at room and elevated temperatures, Ceram. Int. 43 (2017) 13869–13874, https://doi.org/10.1016/j.ceramint.2017.07.110.
[46] U. Schmitt-Radloff, F. Kern, R. Gadow, Manufacturing of electrical discharge machinable ZTA-TiC - hot pressing vs. spark plasma sintering, J. Eur. Ceram. Soc. 38 (2018) 3585–3594, https://doi.org/10.1016/j.jeurceramsoc.2018.03.025.
[47] R. Landfried, F. Kern, W. Burger, W. Leonhardt, R. Gadow, Wire-EDM of ZTA-TiC composites with variable content ofelectrically conductive phase, Key Eng. Mater. 504–506 (2012) 1165–1170. https://doi.org/10.4028/www.scientific.net/KEM.504-506.1165.
[48] W. Voigt, Ueber die Beziehung zwischen den beiden Elasticitätsconstanten isotroper Körper, Ann. Phys. Berlin 274 (1889) 573–587, https://doi.org/10.1002/andp.18892741206.
[49] A. Reuss, Berechnung der fließgrenze von mischkristallen auf grund der plastizitätsbedingung für einkristalle, Z. Angew. Math. Mech. 9 (1929) 49–58, https://doi.org/10.1002/zamm.19290090104.
[50] K. Niihara, A fracture mechanics analysis of indentation-induced palmqvist crack in ceramics, J. Mater. Sci. Lett. 2 (1983) 221–223, https://doi.org/10.1007/BF00725625.
[51] Y.L. Li, T. Ishigaki, Synthesis and structural characterization of titanium oxides and composites by thermal plasma oxidation of titanium carbide, Thin Solid Films 407 (2002) 79–85, https://doi.org/10.1016/S0040-6090(02)00016-0.
[52] Z.K. Zhao, Y.P. Song, Z.M. Feng, Study on the migration law of unmelted WC particles during the process of centrifugal casting, Adv. Mater. Res. 320 (2011) 394–398. https://doi.org/10.4028/www.scientific.net/AMR.320.394.
[53] Z.K. Zhao, Y.P. Song, Z.M. Feng, Analysis on the distribution law of WC particles during centrifugal casting process, Appl. Mech. Mater. 117–119 (2012) 1610–1613. https://doi.org/10.4028/www.scientific.net/AMM.117-119.1610.
[54] L. Sergij, L. Lakiza, Stable and metastable phase relations in the system alumina-zirconia-yttria, J. Am. Ceram. Soc. 4 (1997) 893–902, https://doi.org/10.1111/j.1151-2916.1997.tb02919.x.
[55] V.M. Orera, J.I. Peña, P.B. Oliete, R.I. Merino, A. Larrea, Growth of eutectic ceramic structures by directional solidification methods, J. Cryst. Growth 360 (2012) 99–104, https://doi.org/10.1016/j.jcrysgro.2011.11.056.
[56] V.M. Orera, R.I. Merino, J.A. Pardo, A. Larrea, J.I. Peña, C. Gonzalez, Microstructure and physical properties of some oxide eutectic composites processed by directional solidification, Acta Mater. 48 (2000) 4683–4689, https://doi.org/10.1016/S1359-6454(00)00258-5.
[57] H.J. Su, Q. Su, J. Zhang, K.C. Wei, B. Yao, W.D. Ma, G.R. Fan, M. Guo, L. Liu, H. Bai, H.Z. Fu, Microstructures and mechanical properties of directionally solidified Al_2O_3/$GdAlO_3$ eutectic ceramic by laser floating zone melting with high temperature gradient, J. Eur. Ceram. Soc. 37 (2017) 1617–1626, https://doi.org/10.1016/j.jeurceramsoc.2016.11.041.
[58] Q. Ren, H.J. Su, J. Zhang, G.R. Fan, Z. Lu, W.D. Ma, E.Y. Wang, H.F. Liu, J.F. Ren, L. Liu, Microstructure transition and selection of Al_2O_3/$Er_3Al_5O_{12}$/ZrO_2 ternary eutectic ceramics from micronscale to nanoscale: the effect of rapid solidification, Ceram. Int. 44 (2018) 2611–2614, https://doi.org/10.1016/j.ceramint.2017.10.202.

[59] A.J. Shahani, X.H. Xiao, P.W. Voorhees, The mechanism of eutectic growth in highly anisotropic materials, Nat. Commun. 7 (2016), 12953, https://doi.org/10.1038/ncomms12953.
[60] L.S. Fu, X.S. Fu, G.Q. Chen, W.B. Han, W.L. Zhou, Tailoring the morphology in Y_2O_3 doped melt-grown Al_2O_3/ZrO_2 eutectic ceramic, Scripta Mater. 129 (2017) 20–24, https://doi.org/10.1016/j.scriptamat.2016.10.024.
[61] N.K. Tolochko, Y.V. Khlopkov, S.E. Mozzharov, M.B. Ignatiev, T. Laoui, V.I. Titov, Absorptance of powder materials suitable for laser sintering, Rapid Prototyp. J. 6 (2000) 155–161, https://doi.org/10.1108/13552540010337029.
[62] Q. Ren, H.J. Su, J. Zhang, H.F. Liu, D. Zhao, G.R. Fan, M. Guo, L. Liu, H.Z. Fu, Eutectic growth behavior with regular arrangement in the faceted $Al_2O_3/Er_3Al_5O_{12}$ irregular eutectic system at low growth rate, Scripta Mater. 162 (2019) 49–53, https://doi.org/10.1016/j.scriptamat.2018.10.030.
[63] D.J. Fisher, W. Kurz, A theory of branching limited growth of irregular eutectics, Acta metal 28 (1980) 777–794, https://doi.org/10.1016/0001-6160(80)90155-8.
[64] P. Magnin, W. Kurz, An analytical model of irregular eutectic growth and its application to Fe-C, Acta metal 35 (1987) 1119–1128, https://doi.org/10.1016/0001-6160(87)90059-9.
[65] M.N. Ahsan, R. Bradley, A.J. Pinkerton, Microcomputed tomography analysis of intralayer porosity generation in laser direct metal deposition and its causes, J. Laser Appl. 23 (2011), 22009, https://doi.org/10.2351/1.3582311.
[66] P.A. Kobryn, E.H. Moore, S.L. Semiatin, The effect of laser power and traverse speed on microstructure, porosity, and build height in laser-deposited Ti-6Al-4V, Scripta Mater. 43 (2000) 299–305, https://doi.org/10.1016/S1359-6462(00)00408-5.
[67] Y.F. Huang, D.J. Wu, D.K. Zhao, F.Y. Niu, G.Y. Ma, Investigation of melt-growth alumina/aluminum titanate composite ceramics prepared by directed energy deposition, Int. J. Extreme. Manuf. 3 (2021), 35101, https://doi.org/10.1088/2631-7990/abf71a.
[68] S.J. Wolff, H. Wang, B. Gould, N. Parab, Z.H. Wu, C. Zhao, In situ X-ray imaging of pore formation mechanisms and dynamics in laser powder-blown directed energy deposition additive manufacturing, Int. J. Mach. Tool Manufact. 166 (2021), 103743, https://doi.org/10.1016/j.ijmachtools.2021.103743.
[69] K.W. Chae, D.Y. Kim, B.C. Kim, K.B. Kim, Effect of Y_2O_3 additions on the densification of an Al_2O_3–TiC composite, J. Am. Ceram. Soc. 76 (1993) 1857–1860, https://doi.org/10.1111/j.1151-2916.1993.tb06660.x.
[70] Y.W. Kim, J.G. Lee, Pressureless sintering of Alumina-Titanium carbide composites, J. Am. Ceram. Soc. 72 (1989) 1333–1337, https://doi.org/10.1111/j.1151-2916.1989.tb07647.x.
[71] F.Y. Niu, D.J. Wu, S. Yan, G.Y. Ma, B. Zhang, Process Optimization for suppressing cracks in laser engineered net shaping of Al_2O_3 Ceramics, JOM 69 (2017) 557–562, https://doi.org/10.1007/s11837-016-2191-8.
[72] J. Llorca, J.Y. Pastor, P. Poza, Influence of the Y_2O_3 content and temperature on the mechanical properties of Melt-Grown Al_2O_3-ZrO_2 eutectics, J. Am. Ceram. Soc. 87 (2004) 633–639, https://doi.org/10.1111/j.1551-2916.2004.00633.x.
[73] J.H. Gong, H.Z. Miao, Z. Zhao, The influence of TiC-particle-size on the fracture toughness of Al_2O_3-30 wt.%TiC composites, J. Eur. Ceram. Soc. 21 (2001) 2377–2381, https://doi.org/10.1016/S0955-2219(01)00206-0.
[74] R.W. Davidge, Mechanical Behaviour of Ceramics, Cambridge UP, Cambridge; New York, 1979.
[75] M. Swain, Toughening Mechanisms for Ceramics, ICF7, 1989, pp. 3739–3786.
[76] Y. Zhou, Science of Ceramic Material, second ed., Science Press, Beijing, 2004.
[77] D.J. Wu, Y.F. Huang, F.Y. Niu, G.Y. Ma, S. Yan, C.J. Li, Effects of TiO_2 doping on microstructure and properties of directed laser deposition alumina/aluminum titanate composites, Virtual Phys. Prototyp. 14 (2019) 371–381, https://doi.org/10.1080/17452759.2019.1622987.
[78] D.K. Zhao, D.J. Wu, J. Shi, F.Y. Niu, G.Y. Ma, Microstructure and mechanical properties of melt-grown alumina-mullite/glass composites fabricated by directed laser deposition, J. Adv. Ceram. 11 (2022) 75–93, https://doi.org/10.1007/s40145-021-0518-6.
[79] V.K. Balla, S. Bose, A. Bandyopadhyay, Processing of bulk alumina ceramics using laser engineered net shaping, Int. J. Appl. Ceram. Technol. 5 (2008) 234–242, https://doi.org/10.1111/j.1744-7402.2008.02202.x.
[80] Y.H. Ma, J.H. Ouyang, Z.G. Wang, A. Henniche, Y.H. Wang, Y.J. Wang, Z.G. Liu, Insights into intragranular precipitation and strengthening effect in $Al_2O_3/SmAlO_3$ ceramic with eutectic composition, Mater. Sci. Eng. A-Struct. Mater. Prop. Microstruct. Process. 754 (2019) 382–398, https://doi.org/10.1016/j.msea.2019.03.091.
[81] Y.H. Ma, Z.G. Wang, J.H. Ouyang, J.D. Shen, L. Feng, Y.J. Wang, In-situ microcantilever deflection to evaluate the interfacial fracture properties of binary $Al_2O_3/SmAlO_3$ eutectic, J. Eur. Ceram. Soc. 39 (2019) 3277–3282, https://doi.org/10.1016/j.jeurceramsoc.2019.04.016.
[82] Y.H. Ma, Z.G. Wang, Z.G. Wang, J.D. Shen, A. Henniche, Y.H. Wang, Y.J. Wang, Microstructural toughening mechanisms in nanostructured $Al_2O_3/GdAlO_3$ eutectic composite studied using in situ microscale fracture experiments, J. Eur. Ceram. Soc. 40 (2020) 3148–3157, https://doi.org/10.1016/j.jeurceramsoc.2020.02.042.
[83] L. Mazerolles, N. Piquet, M.F. Trichet, L. Perrière, D. Boivin, M. Parlier, New microstructures in ceramic materials from the melt for high temperature applications, Aero. Sci. Technol. 12 (2008) 499–505, https://doi.org/10.1016/j.ast.2007.12.002.
[84] K. Hirano, Application of eutectic composites to gas turbine system and fundamental fracture properties up to 1700 °C, J. Eur. Ceram. Soc. 25 (2005) 1191–1199, https://doi.org/10.1016/j.jeurceramsoc.2005.01.003.